Analysis of the Ultraviolet Absorption Cross Sections of Six Isotopically Substituted Nitrous Oxide Species Using 3D Wave Packet Propagation†

Shinkoh Nanbu*,‡ and Matthew S. Johnson§

Computer Center, Institute for Molecular Science, Myodaiji Okazaki 444-8585, Japan and Department of Chemistry, University of Copenhagen, Copenhagen, Denmark

Received: March 15, 2004; In Final Form: June 10, 2004

The ultraviolet absorption cross sections of six isotopically substituted nitrous oxide species ($^{14}N^{14}N^{16}O$, $^{14}N^{14}N^{17}O$,$^{14}N^{14}N^{18}O$,$^{14}N^{15}N^{16}O$, $^{15}N^{14}N^{16}O$, and $^{15}N^{15}N^{16}O$) were computed using the wave packet propagation technique to explore the influence of excited-state dynamics, transition dipole surface, and initial vibrational state. Three-dimensional potential energy surfaces for the electronic states of N_2O related to the experimentally observed photoabsorption between 170 and 220 nm were calculated using the ab initio molecular orbital configuration interaction method. The transition dipole moment surfaces between these states were also calculated. Numerous wave packet simulations were carried out and used to calculate the temperature-dependent photodissociation cross sections of the six isotopically substituted species. The photolytic isotopic fractionation constants determined using the calculated cross sections are in good agreement with recent experiments. The results show that, in addition to the effect of the changed shape of the ground-state vibrational wave function with isotopic substitution, photodissociation dynamics play a central role in determining isotopic fractionation constants.

1. Introduction

Nitrous oxide (N_2O) is the most abundant nitrogen-containing species in the atmosphere after molecular nitrogen. It is labile relative to the extremely inert N_2 and thus plays a central role in the biogeochemical nitrogen cycle. N_2O is one of the main greenhouse gases,[1,2] and its oxidation in the stratosphere is the main source of ozone-depleting nitrogen oxides.[3,4] The mole fraction of N_2O in the atmosphere is ca. 320 ppb and is increasing by 0.8 ppb/yr, with an overall increase of ∼17% relative to preindustrial levels.[1] The source of atmospheric N_2O is mainly microbes in the soil and oceans, and its production is stimulated by agricultural fertilizer. Because emissions are diffuse they are difficult to estimate, resulting in an effort to constrain the atmospheric budget of nitrous oxide using isotopic analysis. The mass balance equation links the atmospheric distribution of isotopically distinct N_2O species, the isotopic enrichment of emissions and possible in situ sources, and the fractionation resulting from photochemical loss.[5,6] Isotopically substituted species' distributions have been measured in numerous field studies, using the naturally occurring stable isotopes ^{14}N and ^{15}N and ^{16}O, ^{17}O, and ^{18}O.[7−10] The most important isotopic analogues are $^{14}N^{14}N^{16}O$ (abbreviated 446), 456, 546, 556, 447, and 448.

The main sources of nitrous oxide, bacteria in the soil and ocean, produce N_2O depleted in the heavy isotopes of N and O relative to the troposphere.[9] In contrast to its diffuse emission, the loss of nitrous oxide from the atmosphere is very simple, involving photolysis in the stratospheric UV window (90%):

$$N_2O(1^1\Sigma^+) + h\nu(\lambda \text{ ca. } 205 \text{ nm}) \rightarrow N_2(1^1\Sigma_g^+) + O(^1D) \quad (1.1)$$

and oxidation by $O(^1D)$ (10%).[6,11] Reaction 1.1 occurs on the low energy side of the first electronic absorption band, which is a broad peak centered at 182 nm with a small amount of vibrational structure on the high energy side.[12,13] The quantum yield of reaction 1.1 is unity. Photolysis experiments at 185 nm,[14] in addition to cross section measurements of 446, 456, 546, and 556 between 173 and 197 nm[15] indicated that reaction 1.1 does not result in significant isotopic fractionation, implying a large and fundamental problem in our understanding of the atmospheric N_2O budget. Large additional sources of the isotopically enriched N_2O were therefore proposed (see, for example, ref 16). However, in 1997 Yung and Miller presented the zero point energy (ZPE) model,[17] which made clear that photolysis could result in significant isotopic fractionation. In this model, the position of the absorption band of an isotopically substituted species is taken to be that of the main species shifted by the change in vibrational ZPE. The ZPE model incorporates the invariance of the potential energy surfaces to isotopic substitution (Born−Oppenheimer approximation) and concludes that since the excited state is repulsive, increasing the vertical excitation energy by the ZPE change can approximate the isotope effect. Atmospheric photolysis via reaction 1.1 occurs away from the maximum, and so a small shift of the band position would result in a significantly slower photolysis rate for isotopically heavy species, thus removing the imbalance in the isotopic budget and the need for exotic in situ sources. Subsequent experiments showed isotopic enrichments about twice those predicted by the ZPE model,[18] although qualitative agreement was observed. An effort was made by Billing and co-workers in 2001 to account for the difference between the ZPE model and experiment using a first-principles approach. The Hermite Propagator (HP) model[19,20] incorporated the effects

† Part of the "Gert D. Billing Memorial Issue".

* Author to whom correspondence should be addressed. Phone: +81-564-55-7468. Fax: +81-564-55-7025. E-mail: nanbu@ims.ac.jp.

‡ Institute for Molecular Science.

§ University of Copenhagen.

10.1021/jp048853r CCC: $27.50
Published on Web 08/04/2004

of the thermal distribution of vibrational states in the sample, transition dipole surface[21] and excited-state dynamics and gave better agreement with experiments and field studies. The HP model results were used to describe photolytic fractionation in a 3D atmospheric general circulation model resulting in a description of isotopic fractionation in the stratospheric sink reactions[6] and predicted isotopologue and isotopomer distributions in remarkably good agreement with field studies. However, the HP model could not give a complete description of the photodissociation process since at that time the best available PESs only included two degrees of freedom (Jacobi coordinates with a fixed N_2 bond distance).[21] The two-dimensional model is not unreasonable since the N_2 bond distance contracts less than 3% (from 1.128 Å in N_2O to 1.10 Å in N_2) during the photodissociation process and because reaction 1.1 produces vibrationally cold N_2.[22] Blake, Yung, and co-workers have recently published a semiempirical model for estimating the effect of isotopic substitution on UV absorption spectra.[23,24] This theory goes beyond the ZPE theory by considering the theory for the classical cross section,[25,26] which combines a Wigner distribution function and the reflection principle. Changes in the shape of the ground-state vibrational wave function due to isotopic substitution are linked to shifts in the UV absorption spectrum via the reflection principle. A few parameters describing the excited-state surface are determined by comparing the initial vibrational wave function to the measured absorption spectrum of the main isotopic species. The model is useful for estimating the isotopic fractionation in small molecules with a short-lived excited state in the region of the absorption maximum; however, the model simplifies the dynamics of the system on the excited-state surface. As small systems such as N_2O are amenable to full quantum dynamical calculations, the present study was undertaken to explore the effect of dynamics on the full three-dimensional potential energy surface in addition to the effects of the initial vibrational state and the transition dipole surface.

Nitrous oxide has attracted the attention of theorists[21,27,28] and experimentalists[29−32] in chemical physics for a number of reasons unrelated to its role in the atmosphere. Photodissociation of N_2O is used as a source of excited $O(^1D)$ atoms in molecular beam and kinetics studies. Moreover, since N_2O is chemically stable and the branching ratio for $O(^1D)$ dominates the other two channels, this process is a benchmark system for half-collisions in reaction dynamics. In particular, determination of the rotational distribution of the N_2 fragments is an important research topic and the subject of a number of theoretical and experimental studies.[29−32]

Section 2 outlines the ab initio molecular orbital (MO) configuration interaction (CI) methods used in our determination of the global potential energy surfaces, as well as the wave packet dynamics used to obtain the photodissociation cross sections. Section 3 discusses the potential energy surfaces obtained for the ground and excited states, photodissociation cross sections, and isotopic fractionation factors, comparing them with experimental data. Section 4 summarizes our results.

2. Theoretical Methods

Ab Initio MO CI Calculations. CI calculations were performed at a similar level to that used by Brown et al.[21] The main difference was that the aug-cc-pVTZ (diffusion-function-augmented, correlation consistent, polarized valence, triple-ζ) basis set was used[33] and that a greater number of active space orbitals in the CI and complete active space self-consistent field (CASSCF) calculations were used.

The MOs and electronic configuration for the ground state at its equilibrium geometry were calculated to be as follows:

$$(1a')^2(2a')^2(3a')^2(4a')^2(5a')^2(6a')^2(7a')^2(1a'')^2(8a')^2(2a'')^2$$

$$(9a')^2(10a')^0(3a'')^0(11a')^0(12a')\cdots\cdots(11A')$$

where the key valence orbitals are 7a′: NNO σ bond, $\sigma_{NN} + \sigma_{NO}$; 8a′ and 1a″: NNO π bond, $\pi_{NN} + \pi_{NO}$; 9a′ and 2a″: NN π and NO π^* bonds, $\pi_{NN} + \pi^*_{NO}$; 10a′ and 3a″: NN π^* and NO π^* bonds, $\pi^*_{NN} + \pi^*_{NO}$; 11a′: NN σ and NO σ^* bonds, $\sigma_{NN} + \sigma^*_{NO}$; and 12a′: NN σ^* and NO σ^* bonds, $\sigma^*_{NN} + \sigma^*_{NO}$. The MOs used in the CI calculations are determined by CASSCF calculations. The active space orbitals for the CASSCF calculations were chosen as follows: $[(6a')(7a')(1a'')(8a')(2a'')(9a')(3a'')(10a')\ (11a')]^{12}$.

To obtain the MOs necessary to describe the excited states correlated with $O(^1D) + N_2(\tilde{X}^1\Sigma_g^+)$, state-averaged CASSCF calculations for three A' and two A'' states were performed. The natural orbitals obtained from the CASSCF calculation were used in the final internally contracted multireference configuration interaction (MRCI) calculations.[34,35] The active space of the MRCI calculation was the same as that of CASSCF, and the configuration state functions (CSFs) were generated by single and double excitations with respect to the reference configurations used in the CASSCF calculation. Moreover, the Davidson correction for the MRCI calculation was employed to include correlation energy due to higher excitations.[36−38] The total number of configurations after the internal contraction was typically around 6 000 000 for A' symmetry. The potential energy surfaces (PESs) for the ground electronic state ($1^1A'$) and the next two electronically excited singlet states ($2^1A'$ and 1^1A) were obtained. The transition dipole moments between these states were evaluated from the CI wave functions. The interpolant moving-least-squares (IMLS) method combined with the Shepard interpolation was used to determine the global PESs and the dipole surfaces in the present work.[39] The parameters a and p used to determine the weighting functions (see eq 6 of ref 39) were chosen to be $a = 0.03$ and $p = 3$. The final number of data-points was 1900. All of the ab initio calculations were performed using the MOLPRO 2000.3 program package.[40] The calculations were carried out on the SGI Origin2800 computer of the Research Center for Computational Science of The Okazaki National Institutes. Each data point required about 16 h of CPU time on a single CPU. Using parallel processing with 64 CPUs, it was possible to determine all of the potential energy data over the course of 2 months.

Wave Packet Dynamics. The wave packet propagation technique used in the present work was the "real wave packet" method.[41] Jacobi coordinates were employed to describe the relative positions of the three nuclei in the body fixed plane; R is the distance between the oxygen and the center of mass of N_2, r is the bond length of the N_2 molecule, and θ is the angle between the vectors $\boldsymbol{R}$ and $\boldsymbol{r}$. The wave packet is represented using evenly spaced grids in R and r and a Legendre basis set in $\cos(\theta)$. The radial degree of freedom was taken into consideration in choosing the grid parameters: ($N_R = 255$, $R_{min} = 1.0\ a_0$, $R_{max} = 12.0\ a_0$) and ($N_r = 143$, $r_{min} = 1.0\ a_0$, $r_{max} = 10.0\ a_0$), where N is the number of grid points and a_0 is the Bohr radius. One hundred Legendre functions were used for the angular coordinate. The absorption potential used in the real wave packet propagation is taken as (cf. ref 41) $A(x) = \exp[-C_{abs}(x - x_{abs})^2]$ for $x > x_{abs}$, where $x = R$ or r, $x_{abs} = 8.0\ a_0$ and $C_{abs} = 0.25$.

TABLE 1: Spectroscopic Constants

	this work	Brown et al.[a]	Hopper[b]	expt
R_{NO} (A)	1.180			1.185[c]
R_{NN} (A)	1.129			1.127[c]
θ_e (<NNO,deg)	180.0			180.0
D_0 (eV)	3.617			
D_e (eV)	3.610	3.487	3.120	3.785[d]

[a] MRCI calculated using augmented correlation consistent valence double-ζ (av dz) basis set; however, the two-dimensional model was used fixing the N_2 distance at the experimental data, ref 21. [b] Ref 27. [c] Ref 43. [d] Ref 44.

To simulate the photodissociation process, one must determine the initial wave packet correctly. In the time-dependent formulation, the product of the transition dipole moment function with the bound-state initial wave function gives the initial wave function

$$\Phi_{init}(R,r,\theta; t = 0) = \mu(R,r,\theta)\Psi_{bound}(R,r,\theta) \qquad (2.1)$$

where $\mu(R,r,\theta)$ is the transition dipole moment function for the electronic transition, and $\Psi_{bound}(R,r,\theta)$is the initial bound state. The resulting wave function $\Phi_{init}(R,r,\theta; t = 0)$ is propagated on the electronically excited potential energy surface. Therefore, we have calculated the wave functions on the electronic ground state surface using a Hamiltonian matrix similar to that of the wave packet propagation; the PES was replaced with that of the electronic ground state and the implicitly restarted Lanczos method in ARPACK[42] was used to diagonalize the matrix. According to the Lanczos method, one acts repeatedly with the Hamiltonian on a vector, for example, that for wave packet propagation. This method has been shown to be an efficient way of computing a few eigenvalues and corresponding eigenvectors of large, sparse matrices.

After determining the initial wave packet, it was evolved with time on the excited state potential energy surface, and finally the autocorrelation function was computed by numerically integrating the product of the initial wave packet and the evolving wave packet at each time step. The total photodissociation cross section as a function of excitation energy was calculated as the Fourier transform of the autocorrelation function as a function of time. In SI units,

$$\sigma^{tot}(\nu) = \frac{\pi\nu}{3c\epsilon_0\hbar}\int_{-\infty}^{\infty} dt \exp[i(E_I + h\nu)t/\hbar]A(t) \qquad (2.2)$$

where $A(t)$ is the autocorrelation function, E_I is the energy of the initial bound state, and $h\nu$ is the energy of the incident light. In the present work, the photodissociation cross sections were computed assuming the total angular momentum $J = 0$ (with the exception of the $(0,1^{|1|},0)$ state).

3. Results and Discussion

Potential Energy Surfaces and Transition Dipole Moment Functions. Table 1 tabulates the experimental data and the theoretical results for the equilibrium geometry and the dissociation energy in the electronic ground state. Our results are in better agreement with the experimental data than previous theoretical data. The vibrational frequencies for the isotopically substituted molecules are listed in Table 2. According to the accepted convention, we use ν_1, ν_2, and ν_3 to denote vibrational quanta for the symmetric stretching (resembling NO stretching), bending, and anti-symmetric stretching (resembling NN stretching) modes, respectively. On the other hand, since the vibrational angular momentum l is expected to be an almost-good quantum number in the linear molecule, the allowed values of l are connected with the bending quantum number, $l = -\nu_2, -\nu_2 + 2, ..., +\nu_2$; moreover, the allowed values of the total angular momentum quantum number J are connected with l, $J = |l|, |l| + 1, ...$ Therefore, to obtain the initial wave packet for the $(0,1^{|1|},0)$ level, we performed the rovibrational calculation with $J = 1$. In the table, we indicate $|l|$ as a superscript on the bending quantum number ν_2. The theoretical results did a remarkably good job of reproducing the changes in ZPE found by experiment. The ordering of the fundamental frequency of the ν_1 mode is 446 > 447 > 546 > 448 > 456 > 556 in the calculation, whereas the experimental ordering is 446 > 456 > 546 > 556 > 447 > 448. The largest quantitative difference between theoretical results and the experimental data is in the ν_3 fundamental frequencies. However, this is reasonable from a theoretical point of view because the correlation energy in our MRCI calculation was not enough to describe the potential energy surface, particularly with regards to the N_2 bond. Antibonding MOs for N_2 were not included in the CAS space. All theoretical results underestimate the experimental data by $\Delta E < 90$ cm^{-1}.

TABLE 2: Vibrational Frequencies in the Ground Electronic State (cm^{-1})

	$^{14}N^{14}N^{16}O$		$^{14}N^{14}N^{17}O$		$^{14}N^{14}N^{18}O$	
$(\nu_1,\nu_2^{\|l\|},\nu_3)$	this work	exp	this work	exp	this work	exp
$(0,0^0,0)$	0.00	0.00	0.00	0.00	0.00	0.00
$(0,1^1,0)$	615.58	588.768[b]	613.04	586.362[d]	610.79	584.225[d]
$(0,2^0,0)$	1134.29	1168.13[a]	1113.85		1095.08	
$(1,0^0,0)$	1234.99	1284.903[a]	1228.69	1264.704[a]	1223.33	1246.885[a]
$(0,0^0,1)$	2167.64	2223.757[c]	2163.87	2220.074[c]	2160.37	2216.711[c]
ZPE	2306.76	2343.10	2292.41	2328.75	2279.52	2316.02
ΔZPE	0.00	0.00	14.35	14.35	27.24	27.08
	$^{14}N^{15}N^{16}O$		$^{15}N^{14}N^{16}O$		$^{15}N^{15}N^{16}O$	
$(\nu_1,\nu_2^{\|l\|},\nu_3)$	this work	exp	this work	exp	this work	exp
$(0,0^0,0)$	0.00	0.00	0.00	0.00	0.00	0.00
$(0,1^1,0)$	601.77	575.434[b]	611.98	585.312[b]	598.08	571.894[d]
$(0,2^0,0)$	1130.75		1119.12		1116.15	
$(1,0^0,0)$	1208.89	1280.354[a]	1227.50	1269.892[a]	1201.04	1265.334[a]
$(0,0^0,1)$	2122.60	2177.657[c]	2146.01	2201.605[c]	2100.20	2154.726[c]
ZPE	2268.12	2304.44	2284.46	2321.06	2245.55	2281.92
ΔZPE	38.64	38.66	22.30	22.04	61.21	61.18

[a] Ref 45. [b] Ref 46. [c] Ref 47. [d] Ref 48.

Our interest in this paper is the photodissociation process relative to $O(^1D) + N_2(\tilde{X}^1\Sigma_g^+)$, and the calculation must be performed within the framework of available computational resources. In this sense, we had to keep the active space smaller than the full active space, especially for N_2 bond-breaking; the 12a′ orbital characterized by NN σ^* and NO σ^* bonds, $\sigma^*_{NN} + \sigma^*_{NO}$ was not included in the active space of the CASSCF and MRCI calculations. This restriction could lead to an underestimation of the ν_3 fundamental frequencies. Regarding the order of the ν_1 fundamental frequencies, the effect is due to the mixing of the NO and NN stretching modes because the ν_1 and ν_3 modes have some character of the NO stretching and NN stretching modes, respectively. However, in the case of an almost evenly mass-weighted system like N_2O, these two modes are mixed, as in CO_2. The modes resemble almost symmetric and almost anti-symmetric stretching motions. Thus, the theoretical ν_3 fundamental frequencies came to be smaller than the corresponding experimental frequencies and the order of the sequence for the ν_1 mode was simultaneously affected.

Figure 1a shows the potential energy curves as a function of Jacobi coordinates R at a fixed N_2 bond distance $r = 1.13$ Å and Jacobi coordinate angle $\theta = 0.0°$ (i.e., linear). In all of our potential energy figures, the energy zero is taken to be the minimum energy of the electronic ground state. There are three electronic states, $1^1\Sigma^+$, $1^1\Pi$, and $1^1\Delta$, correlated with the $O(^1D) + N_2(\tilde{X}^1\Sigma_g^+)$ asymptote in $C_{\infty v}$ symmetry. $1^1\Sigma^+$ is the ground state, while the first excited state is $1^1\Sigma^-$. Moreover, the $1^1\Delta$ state closely resembles the $1^1\Sigma^-$ state. The vertical excitation energy between $1^1\Sigma^-$ and $1^1\Sigma^+$ is $T_e = 6.81$ eV, while $T_e(1^1\Delta - 1^1\Sigma^+)$ is 6.97 eV. These values are somewhat lower than the values obtained by Brown and co-workers (see Table 2 of ref 21). As clearly seen in the figure, both the $1^1\Sigma^-$ and the $1^1\Pi$ surfaces cross $1^1\Delta$ at about $R = 2.0$ Å. Once the molecule becomes slightly bent, these crossings are avoided due to Neumann-Wigner's non-crossing rule, resulting in conical intersections. Thus bending distortion on both the $A'(1^1\Delta)$ and $A''(1^1\Sigma^-)$ surfaces leads to prompt adiabatic dissociation into $O(^1D) + N_2(\tilde{X}^1\Sigma_g^+)$ via $A'(1^1\Pi)$ and $A''(1^1\Pi)$. These features are quite similar to the isovalent-electronic system, OCS.[49]

Figure 1b shows the potential energy curves versus θ with $R = 1.8$ Å and $r = 1.13$ Å. The Renner−Teller pair of $1^1\Delta$ splits into the $2^1A'$ and $2^1A''$ states, and an avoided curve crossing between the two lowest A' states is clearly seen to be present. In addition, as discussed in ref 21, there is evidence that the avoided crossing becomes a seam of interaction at around $\theta = 50.0°$ because it holds even for the various geometries which allow R and r to relax; that is, $R \in$ [1.0, 1.2, 1.4, 1.5, 1.6, 1.7, 1.8, 2.0, 2.2, 2.4] Å and $r \in$[0.8, 1.0, 1.13, 1.2, 1.3, 1.4, 1.5, 1.6, 1.8, 2.0] Å. Thus, a non-symmetry-related conical intersection could be located at around the bent geometry. Excitation onto the lower-lying $1^1A''$ and $2^1A'$ states is responsible for the first broad absorption band observed in the UV region.

Figure 1c shows the transition dipole moment functions for the $1^1A''-1^1A'$ and $2^1A'-1^1A'$ transitions as a function of θ with $R = 1.8$ Å and $r = 1.13$ Å. Both of the dipole moments are zero in the linear geometry and are strongly angle dependent. The two dips at around $\theta = 50.0°$ are due to the strong variation of the characters of the CI (i.e., the coefficients of CSFs or the avoided crossing between the two A' states). In contrast, no dip is observed for the $1^1A''-1^1A'$ transition.

The main features of the calculated potential resemble the results obtained by Brown and co-workers, with the exception of the quantitative energetics. As discussed in the next section,

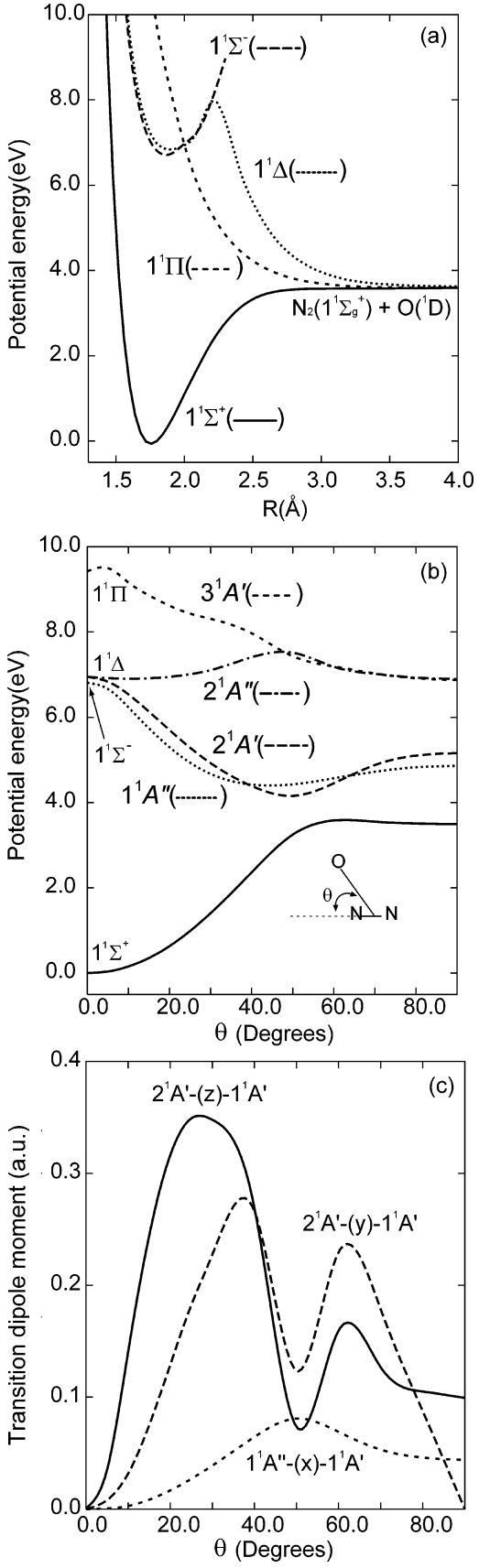

Figure 1. Potential energy curves in the ground and low-lying electronically excited states, and transition dipole moments between the ground state and the low-lying excited states: (a) potentials as a function of R, with $r = 1.13$ Å and $\theta = 0.0°$ (i.e., linear N_2O); (b) potentials as a function of θ, with $R = 1.8$ Å and $r = 1.13$ Å; (c) transition dipole moments as a function of θ, with $R = 1.8$ Å and $r = 1.13$ Å.

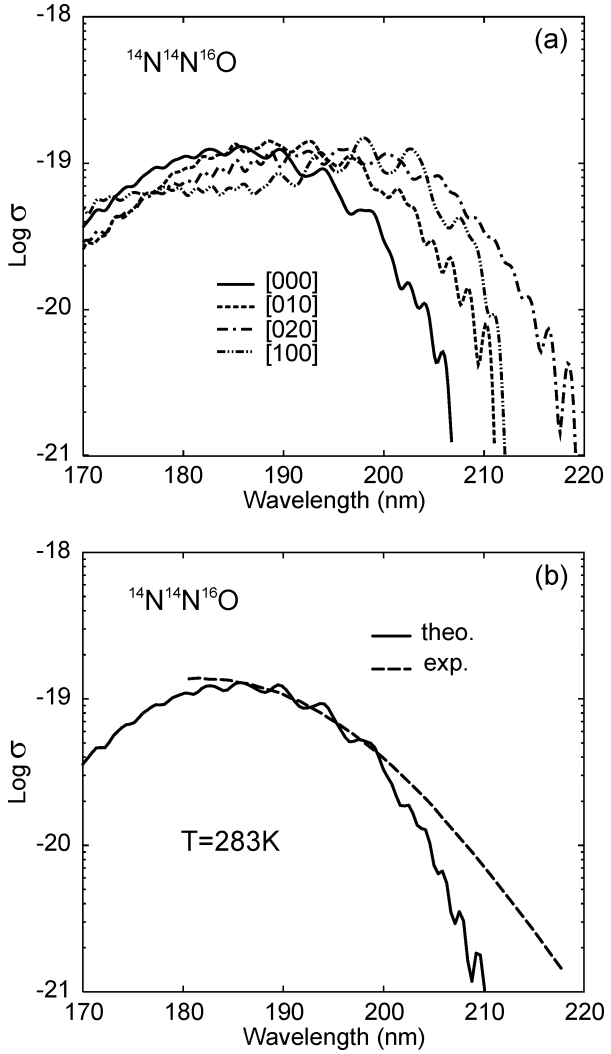

Figure 2. Theoretical and experimental photoabsorption spectra for $^{14}N^{14}N^{16}O$. Cross section units are cm^2 $molecule^{-1}$: dependence of the cross section on the initial vibrational state in the electronic ground state; comparison with the experimental data of ref 12 at $T = 283$ K.

the newly generated 3D potential surfaces and transition functions are used to calculate the theoretical photodissociation cross sections.

Photodissociation Cross Sections. The calculated photodissociation cross sections for $^{14}N^{14}N^{16}O$ are shown in Figure 2a,b. Figure 2a shows the dependence on the initial vibrational state in the electronic ground state. It is clearly seen that the $(0,1^1,0)$ state has the largest cross section at around 190 nm relative to the other states and that the cross sections at longer wavelengths (~215 nm) become larger with bending vibrational excitation, leading to the well-known temperature dependence on the red shoulder of the peak due to vibrational hot bands.[13,15,18] It is interesting to note that the contribution of the $(1,0^0,0)$ state is predicted to be larger than that of the $(0,1^1,0)$ state on the low energy side, although this was not clear in the previous work.[20] Figure 2b shows the Boltzmann-averaged spectrum at 283 K. Vibrational states up to five levels from the zero point vibrational state are taken into account. To reduce the size of the calculation, the angular momentum of the initial and scattering states was taken to be zero. As discussed by Offer and Balint-Kurti, this may effect predictions regarding the final distribution of rotational states in the N_2 fragment;[50] however, the effect on the absolute cross section is not likely to be significant. Since in the newest experiments the absorption spectrum has been

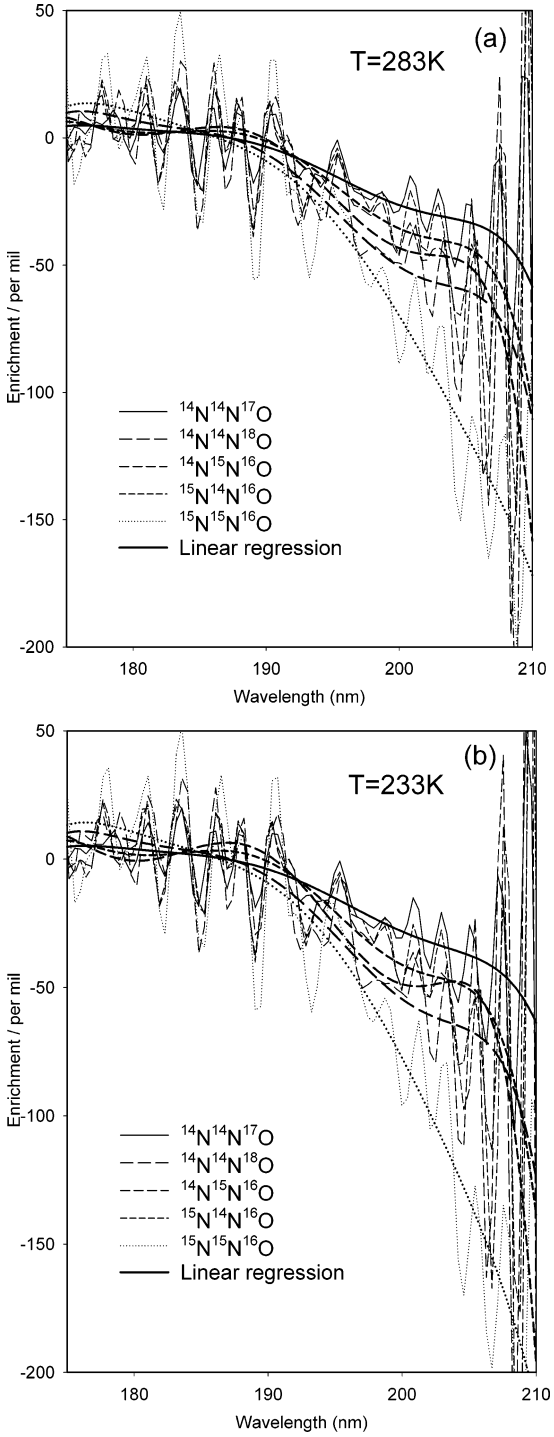

Figure 3. Theoretical isotopic fractionation constants for 447, 448, 456, 546, and 556 at (a) 283 and (b) 233 K.

measured at 283 K, the temperature for the Boltzmann average is chosen to be 283 K.[18] The theoretical results are in good agreement with the newest experimental data, with the exception of some error in the low energy region. We believe that this does not represent a serious problem for our purpose, and it is certainly possible that with more accurate ab initio calculations the error could be fixed. The position of the absorption maximum matches the experimental value, confirming improved values for the energies of the excited surface; in contrast, the 2D theoretical spectrum was offset by 3 nm relative to the experimental value.

Comparison to Experimental Fractionation Constants. Figure 3 shows the theoretical fractionation constant ϵ (also

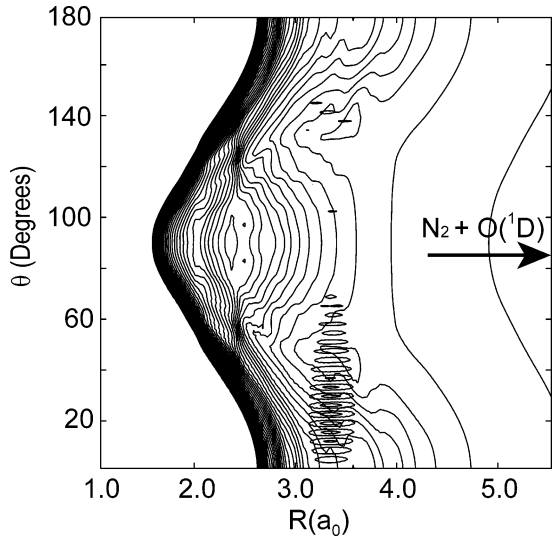

Figure 4. Plot of a Feschbach resonance occurring at an excitation energy of 53 815 cm^{-1} (wavelength 185.82 nm).

called the enrichment factor), which is defined by

$$\epsilon_{ijk} = \frac{\sigma_{ijk}}{\sigma_{446}} - 1 \qquad (3.1)$$

where σ_{ijk} is the cross section of a given isotopically substituted species. The large negative value at longer wavelengths indicates the strong potential for isotopic fractionation in the stratosphere, which occurs in the "UV window" between ca. 197 and 210 nm.[11] The 556 isotopically substituted species shows the strongest fractionation constant of all of the candidates, and the order of the constants is consistent with the experimental data. The fractionation constant for 447 is roughly half that of 448. Comparing the equal-mass isotopomers 456 and 546, the model predicts qualitatively similar fractionations with a surge around 205 nm, quickly falling off to longer wavelengths. The temperature dependence of the fractionation constants can be seen by comparing Figure 3a (283 K) with Figure 3b (233 K). Larger fractionation constants are seen at lower temperatures.[18,20] As seen in the figures, there are strong fluctuations, especially in the lower energy region. This is because the wave packet recurrence predicted by theory is slightly stronger than in the real system. As seen in Figure 4, there is a small local minimum in the bent geometry which is at $R = 3.5\ a_0$ and $\theta = 40°$ and 140°. The minimum occurs at around 5.0 eV (248 nm), and a part of the wave packet is trapped in this region, leading to the observed structure. This phenomena also occurs in the Hartley band of O_3.[51] Spectral analysis was used too analyze the structure more precisely.[52] The wave function associated with the peak energy of the observed structure could be found by re-computing the wave packet propagations and accumulating the sum of the wave packet with a window function after computing the photo-absorption spectra. The wave function corresponding to one of the peaks at $E = 185.82$ nm is shown in Figure 4. Note that we have set $r = 2.44\ a_0$ in this figure. It is clearly seen that the wave function is localized around $R = 3.5\ a_0$ and $\theta = 20°$. This is a Feschbach type resonance in which the energy is temporarily trapped in a transverse bending motion against the dissociation path. However, the structure estimated by our theory is stronger than that of the experiment, probably because of limitations in the potential energy surface. This error, which is not overly pronounced in Figure 2, is amplified by eq 3.1. Therefore, we have chosen to smooth the data using linear regression; polynomial fitting with up to quartic functions was used. The effect of the fitting was to smooth features in the calculated spectra that were finer than ca. 3 nm.

Figure 5 shows the fractionation constants for the 456, 546, and 556 analogues at 283 and 233 K compared to experiments,[18] the ZPE model,[17] the HP model,[20] and the recent model of Blake et al.[24] The agreement for these three isotopically substituted species is satisfactory; however, the calculated fractionation factor drops rapidly in the long wavelength region as compared to the experimental data. This is a consequence of the decrease in the underlying cross sections in the long wavelength region, as shown in Figure 2b. The solution undoubtedly lies in more accurate ab initio calculations for determining the global PESs although that was not possible in this study. It is interesting to note that the calculations do not predict so-called mass independent fractionation of the ^{17}O and ^{18}O isotopologues through photolysis.[6,18] The average fractionation factor of 447 shown in Figure 3 between 197 and 207 nm is 0.517 that of 448, fully in line with "mass-dependent" fractionation.

Figure 5 shows the fractionation constants of the nitrogen isotopically substituted species as a function of wavelength at 283 and 233 K, compared to theory and experiment. In general a curved fractionation constant is predicted, being largest at high energies and dropping rapidly at longer wavelengths. The size of the fractionation constant increases with decreasing temperature. As noted previously, the calculated absolute cross section (cf. Figure 2b) drops below the experimental value; accurate at 200 nm, by 210 nm the calculated values correspond to the experimental values at 220 nm. This is a challenging spectral region; at 220 nm the cross section is only 1% of the maximum. Comparison of this excitation energy (220 nm $\approx$ 5.6 eV) with the cuts through the potential energy surfaces shown in Figure 1a,b shows that the transition in this region involves coupling to continuum states that are distant from the geometry of the ground-state vibrational wave function. While the error could be due to the quality of the PES, other factors will also play a role. The wave packet recurrence is exaggerated due to the local minimum of the $2^1A'$ state linked to the conical intersection; the wave packet could be trapped by the local minimum around $R = 3.5\ a_0$ and $\theta = 40°$, which is shown in Figure 4. Therefore, the strong resonances around 220 nm could be removed by including the nonadiabatic transition around the local minimum since the minimum is located around 5.0 eV. On the other hand, this recurrence is what gives rise to the Feschbach resonance.

It is interesting to compare the results for the equal-mass species 456 and 546. According to the calculation, the photodissociation dynamics lead to a fractionation constant for 546 that is less than half that of 456. The results presented here improve upon the calculations performed on the 2D potential energy surface, especially in the stratospheric UV window region around 205 nm. Significantly, the "bump" in the 2D results for 546 has disappeared, confirming the effect of the frozen N_2 degree of freedom on the 2D calculations. The calculated fractionation constants are high by 10−20‰ in the high energy region. It is seen that the time-independent semi-empirical model does a good job of predicting the observed experimental fractionation constants. Note that improved semi-empirical wavelength-dependent fractionation constants have recently been published.[23]

In the time-dependent formulation[52] there is the possibility for rich dynamical behavior, including Feschbach resonances, as shown in Figure 4. In the case illustrated, occurring at the maximum of the absorption curve, there is a resonance between the dissociation path and bending motion.[51] The lifetime of the excited state is indicated in Figure 6, which presents the flux

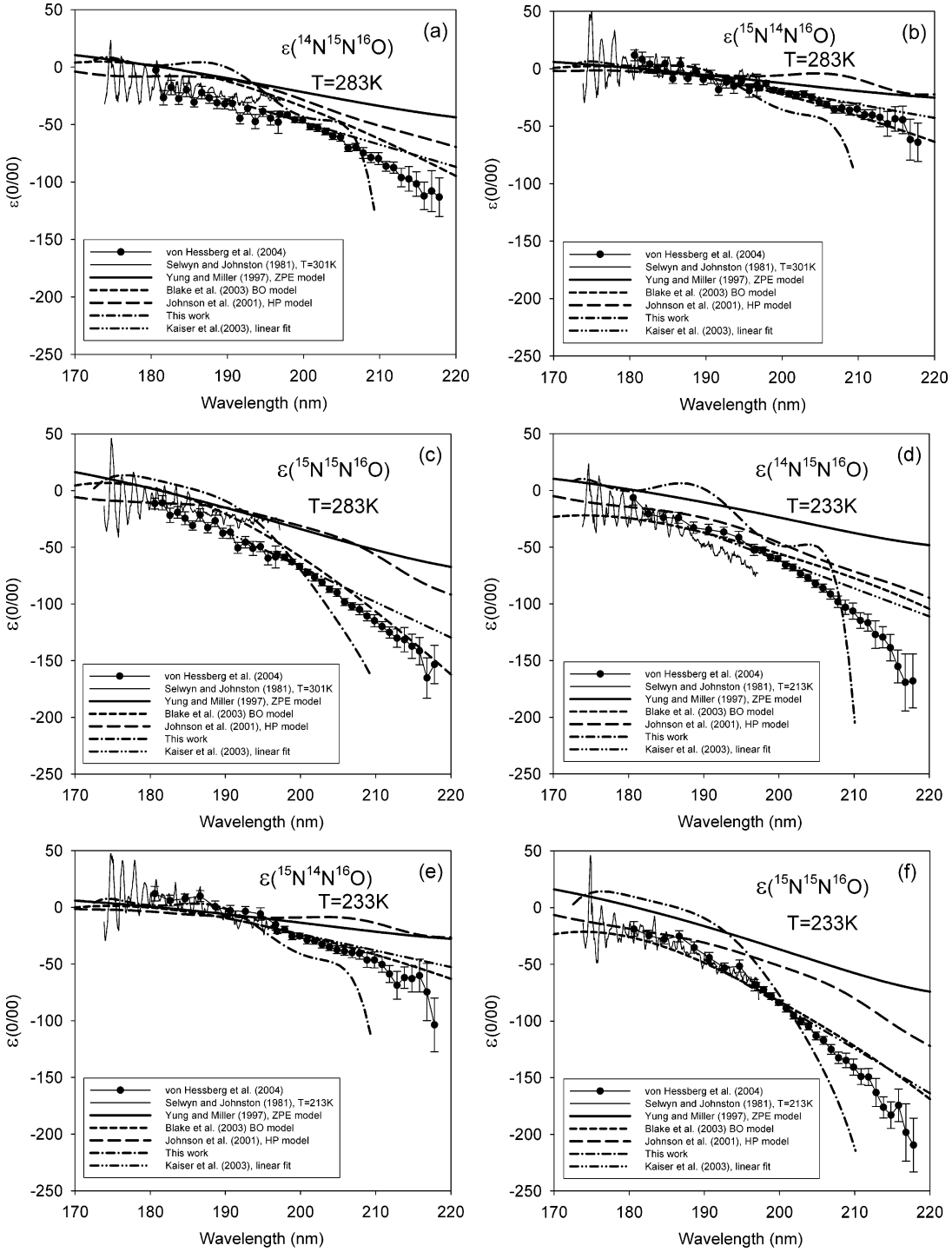

Figure 5. Comparison of the predicted fractionation constants with experiment for the ^{14}N and ^{15}N analogues[15,18,53] and theory.[17,20,23,24] (a) 456 at 283 K. (b) 546 at 283 K. (c) 556 at 283 K. (d) 456 at 233 K. (e) 546 at 233 K. (f) 556 at 233 K.

leaving the computational grid as a function of time. There is a bimodal distribution with a fast component with maximum at ca. 25 fs and a slower component with a lifetime of hundreds of fs with a maximum at ca. 70 fs. The three vibrational frequencies (cf. Table 2) correspond to periods of 27, 54, and 15 fs, respectively. Thus the photodissociation of N_2O has components that are direct, and components that are indirect. This is seen in the experimental spectrum that displays fine structure superimposed on a broad shifted Gaussian continuum.

The rotational distributions of the N_2 fragment are shown in Figure 7. One interesting result is that the predicted slight bimodal distribution in photodissociation from the 0,0,0 state

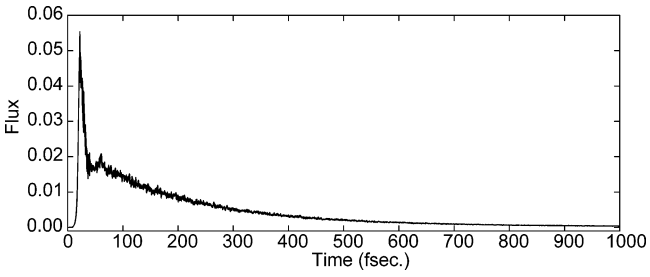

Figure 6. Plot of the population flux leaving the computational grid as a function of time, taken at $R = 4.0$ Å.

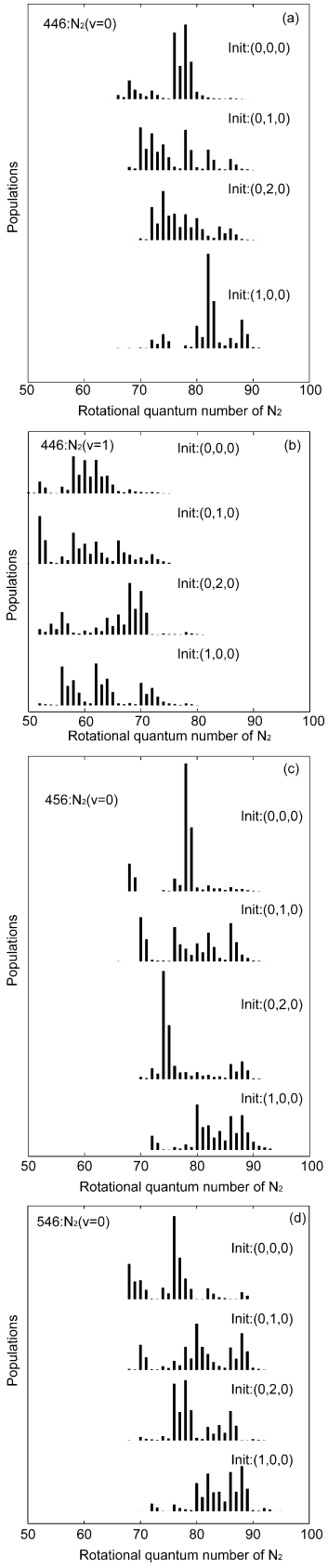

Figure 7. N_2 rotational distributions as calculated by the model. (a) Rotational quantum number of the N_2 fragment originating from 446 isotopically substituted species ($v = 0$). (b) Rotational quantum number of the N_2 fragment originating from 446 isotopically substituted species ($v = 1$). (c) Rotational quantum number of the N_2 fragment originating from 456 isotopically substituted species ($v = 0$). (d) Rotational quantum number of the N_2 fragment originating from 546 isotopically substituted species ($v = 0$).

of 446 grows significantly in 456 and 546. Another is that the degree of rotational excitation grows from 546 to 456; this may be connected with the slightly larger bending excursion of the 456 isotopomer. The predicted rotational distributions match the experimental values very well;[29−32] however, it is likely that the inclusion of rotational selection rules and a Boltzmann distribution of initial rotational states would change the results of the calculation.[50]

4. Concluding Remarks

We determined global ab initio potential energy surfaces for ground $1^1\Sigma^+$ ($1^1A'$), $1^1A''$ and $2^1A'$ electronically excited states. We also determined the transition dipole moment surfaces between the ground and excited states. Using wave packet propagation, the dynamics using the new global PESs and transition dipole moment surfaces provided new information concerning the photodissociation cross sections of six isotopically substituted N_2O species. The theoretical isotopic fractionation factors are in reasonable agreement with recently obtained experimental data. Moreover our results were able to "close the gap" between the ZPE model, the 2D propagation work, and experimental data. Of particular interest was the discovery of the contribution of the vibrational $(1,0^0,0)$ state (like $(0,2^0,0)$), particularly around 205 nm. It should be noted that our surfaces, while generated at a relatively high level of ab initio theory, were still not accurate enough and provided only qualitative agreement with the experimental data. Soon, it is hoped that more accurate PESs will help give us a complete understanding the effect of isotopic substitution on photolysis cross section. In sum, isotope effects are a demanding test of the veracity of theoretical models. Current time-dependent techniques are able to predict the effect of isotopic substitution on absorption cross sections to an accuracy of a few percent.

Acknowledgment. This research was supported in part by the Grant-in-Aid for Scientific Research from the Ministry of Education, Culture, Sports, Science and Technology of Japan. The main part of the computation was carried out using the computer facilities at the Research Center for Computational Science of The Okazaki National Institutes. M.S.J. acknowledges the support of the Danish Natural Science Research Council. This paper is dedicated to the memory of our colleague and friend Professor Gert Due Billing.

References and Notes

(1) Prather, M.; et al. Atmospheric chemistry and greenhouse gases. In *Climate Change 2001*: *The Scientific Basis*; Contribution of Working Group I to the Third Assessment Report of the Intergovernmental Panel on Climate Change; Houghton, J. T., et al., Eds.; Cambridge University Press: New York, 2001; pp 239−287.

(2) Yung, Y. L.; Wang, W. C.; Lacis, A. A. *Geophys. Res. Lett.* **1976**, *3*, 619.

(3) Crutzen, P. J. *Q. J. R. Meteorol. Soc.* **1970**, *96*, 320.

(4) McElroy, M. B.; McConnnell, J. C. *J. Atmos. Sci.* **1971**, *28*, 1095.

(5) Kaiser, J.; Röckmann, T.; Brenninkmeijer, C. A. M.; Crutzen, P. *J. Atmos. Chem. Phys.* **2003**, *3*, 303.

(6) McLinden, C. A.; Prather, M. J.; Johnson, M. S. *J. Geophys. Res.* **2003**, *108* (D8), 4233.

(7) Yoshida, N.; Matsuo, S. *Geochem. J.* **1983**, *17*, 231.

(8) Röckmann, T.; Kaiser, J.; Brenninkmeijer, C. A. M.; Crowley, J. N.; Brochers, R.; Brand, W. A.; Crutzen, P. J. *J. Geophys. Res.* **2001**, *106*, 403.

(9) Kim, K.-R.; Craig, H. *Science* **1993**, *256*, 1855.

(10) Turatti, F.; Griffith, D. W. T.; Wilson, S. R.; Esler, M. B.; Rahn, T.; Zhang, H.; Blake, G. A. *Geophys. Res. Lett.* **2000**, *27*, 2489.

(11) Minschwaner, K.; Salawitch, R. J.; McElroy, M. B. *J. Geophys. Res.* **1993**, *98* (D6), 10543−10561.

(12) Selwyn, G.; Podolske, J.; Johnston, H. S. *Geophys. Res. Lett.* **1977**, *4* (10), 427.

(13) Yoshino, K.; Esmond, J. R.; Parkinson, W. H. *Chem. Phys.* **1997**, *221*, 169.
(14) Johnston, J. C.; Cliff, S. S.; Thiemens, M. H. *J. Geophys. Res.* **1995**, *100* (D8), 16801.
(15) Selwyn, G. S.; Johnston, H. S. *J. Chem. Phys.* **1981**, *74*, 3791.
(16) Zipf, E. C.; Prasad, S. S. *Geophys. Res. Lett.* **1998**, *25* (23), 4333.
(17) Yung, Y. L.; Miller, C. E. *Science* **1997**, *278*, 1778.
(18) von Hessberg, P.; Kaiser, J.; Enghoff, M. B.; McLinden, C. A.; Sorensen, S. L.; Röckmann, T.; Johnson, M. S. *Atmos. Chem. Phys. Discuss.* **2004**, *4*, 2333.
(19) Vijay, A.; Wyatt, R. E.; Billing, G. D. *J. Chem. Phys.* **1999**, *111*, 10794.
(20) Johnson, M. S.; Billing, G. D.; Gruodis, A.; Janssen, H. M. *J. Phys. Chem. A* **2001**, *105*, 8672.
(21) Brown, A.; Jimeno, P.; Balint-Kurti, G. G. *J. Phys. Chem. A* **1999**, *103*, 11089.
(22) Hanisco, T. F.; Kummel, A. C. *J. Phys. Chem. A* **1993**, *97*, 7242.
(23) Morgan, G. C.; Allen, M.; Liang, M. C.; Shia, R. L.; Blake, G. A.; Yung, Y. L. *J. Geophys. Res.* **2004**, *109*(D4), D04305, doi:10.1029/2003JD003402.
(24) Blake, G. A.; Liang, M.-C.; Morgan, C. G.; Yung, Y. L. *Geophys. Res. Lett.* **2003**, *30*, 1656.
(25) Schinke, R. *J. Phys. Chem.* **1986**, *90*, 1742.
(26) Nanbu, S.; Iwata, S. *J. Phys. Chem.* **1992**, *96*, 2103.
(27) Hopper D. G. *J. Chem. Phys.* **1984**, *80*, 4290.
(28) Janssen, M. H. M.; Teule, J. M.; Neyer, D. W.; Chandler, D. W.; Groenenboom, G. C. *Faraday Discuss.* **1999**, *113*, 473.
(29) Suzuki, T.; Katayanagi H.; Mo, Y.; Tonokura, K. *Chem. Phys. Lett.* **1996**, *256*, 90.
(30) Neyer, D. W.; Heck, J. R.; Chandler, D. W. *J. Chem. Phys.* **1999**, *110*, 3411.
(31) Neyer, D. W.; Heck, J. R.; Chandler, D. W.; Teule, J. M.; Janssen, M. H. M. *J. Phys. Chem. A* **1999**, *103*, 10388.
(32) Rijs, A. M.; Backus, E. H. G.; de Lange, C. A.; Janssen M. H. M.; Wang, K.; McKoy V. *J. Chem. Phys.* **2001**, *114*, 9413.
(33) Woon, D. E.; Dunning, T. H., Jr. *J. Chem. Phys.* **1993**, *98*, 1358 and references therein.
(34) Werner, H.-J.; Knowles, P. J. *J. Chem. Phys.* **1988**, *89*, 5803.
(35) Knowles, P. J.; Werner, H.-J. *Chem. Phys. Lett.* **1988**, *145*, 514.
(36) Langhoff, S. R.; Davidson, D. E. *Int. J. Quantum Chem.* **1974**, *8*, 61.
(37) Blomberg, M. R. A.; Siegbahn, P. E. M. *J. Chem. Phys.* **1983**, *78*, 5682.
(38) Simons, J. *J. Phys. Chem.* **1989**, *93*, 626.
(39) Ishida, T.; Schatz, G. C. *Chem. Phys. Lett.* **1999**, *314*, 369.
(40) MOLPRO is a package of ab initio programs written by Werner, H.-J.; Knowles, P. J., with contributions from Amos, R. D.; Berning, A.; Cooper, D. L.; Deegan, M. J. O.; Dobbyn, A. J.; Eckert, F.; Hampel, C.; Leininger, T.; Lindh, R.; Lloyd, A. W.; Meyer, W.; Mura, M. E.; Nicklass, A.; Plamieri, P.; Peterson, K.; Pitzer, R.; Pulay, P.; Rauhut, G.; Schütz, M.; Stoll, H.; Stone, A. J.; Thorsteinsson, T. *Version 2000.3*; See the MOLPRO homepage, http://www.molpro.net.
(41) Gray, S. K.; Balint-Kurti, G. G. *J. Chem. Phys.* **1998**, *108*, 950.
(42) ARPACK is a collection of Fortran77 subroutines designed to solve large scale eigenvalue problems written by Lehoucq, R. B.; Maschhoff, K.; Sorensen, D. C.; Yang, C. Rice University, 1997. See the ARPACK homepage, http://www.caam.rice.edu/software/ARPACK/.
(43) Herzberg, G. *Molecular Spectra & Molecular Structure Vol. III*; Van Nostrand Company: New York, 1945.
(44) Chase, M., Jr.; Davies, C. A.; Downey, J. R., Jr.; Frurip, D. J.; McDonald, R. A.; Syverud, A. N. *JANAF Thermochemical Tables*, 3rd ed.; American Chemical Society: Washington, DC, 1986.
(45) Toth, R. A. *J. Opt. Soc. Am. B.* **1986**, *3*, 1263.
(46) Jolma, K.; Kauppinen, J.; Horneman, V.-M. *J. Mol. Spectrosc.* **1983**, *101*, 278.
(47) Toth, R. A. *J. Opt. Soc. Am. B.* **1987**, *4*, 375.
(48) Amiot, C. *J. Mol. Spectrosc.* **1976**, *59*, 380.
(49) Suzuki, T.; Katayanagi, H.; Nanbu, S.; Aoyagi, M. *J. Chem. Phys.* **1998**, *109*, 5778.
(50) Offer, A. R.; Balint-Kurti, G. G. *J. Chem. Phys.* **1994**, *101*, 10416.
(51) Leforestier, C.; LeQuere, F.; Yamashita, K.; Morokuma, K. *J. Chem. Phys.* **1994**, *101*, 3806.
(52) Feit, M. D.; Fleck, J. A.; Steiger, A. *J. Comput. Phys.* **1982**, *47*, 412.
(53) Kaiser, J.; Röckmann, T.; Brenninkmeijer, C. A. M. *J. Geophys. Res.* **2003**, *108* (D15), 4476,.